Available online at www.sciencedirect.com
ScienceDirect
Journal of Power Sources 159 (2006) 570–585
JOURNAL OF POWER SOURCES
www.elsevier.com/locate/jpowsour

High temperature solid oxide fuel cell integrated with novel allothermal biomass gasification Part I: Modelling and feasibility study

K.D. Panopoulos [a], L.E. Fryda [a], J. Karl [b], S. Poulou [c], E. Kakaras [a,*]

[a] *Laboratory of Steam Boilers and Thermal Plants, School of Mechanical Engineering, Thermal Engineering Section, National Technical University of Athens, 9 Heroon Polytechniou Ave. Zografou 15780, Greece*
[b] *Institute of Thermal Power Systems, Technical University of Munich, Boltzmannstrasse 15, 85747 Garching, Germany*
[c] *Hyperion Systems Engineering Ltd., Nicosia, 1075, Cyprus*

Received 17 March 2005; received in revised form 8 November 2005; accepted 12 December 2005
Available online 24 January 2006

Abstract

Biomass gasification derived fuel gas is a renewable fuel that can be used by high temperature fuel cells. In this two-part work an attempt is made to investigate the integration of a near atmospheric pressure solid oxide fuel cell (SOFC) with a novel allothermal biomass steam gasification process into a combined heat and power (CHP) system of less than MW_e nominal output range. Heat for steam gasification is supplied from SOFC depleted fuel into a fluidised bed combustor via high temperature sodium heat pipes. The integrated system model was built in Aspen Plus™ simulation software and is described in detail. Part I investigates the feasibility and critical aspects of the system based on modelling results.

A low gasification steam to biomass ratio (STBR = 0.6) is used to avoid excess heat demands and to allow effective H_2S high temperature removal. Water vapour is added prior to the anode to avoid carbon deposition. The SOFC off gases adequately provide gasification heat when fuel utilisation factors are <0.75; otherwise extra biomass must be combusted with overall efficiency penalty. For SOFC operation with $U_f = 0.7$ and current density 2500 A m^{-2} the electrical efficiency is estimated at 36% while thermal efficiency at 14%. An exergy analysis is presented in Part II.

Keywords: Modelling; SOFC; Biomass; Gasification; Aspen Plus™

1. Introduction

Biomass is among the most promising renewable energy sources, able to be used by a wide range of small and large scale power production technologies.

There are contradicting opinions whether small or large scale biomass applications are the most promising. Biomass steam cycles operating in the range 5–20 MW_e are now producing most of the bio-electricity around the world. Their electrical efficiency is limited to 20–25% avoiding high capital costs associated with elevated steam properties and complex steam cycle integration. For even larger power plants (i.e. >20 MW_e) the Integrated Gasification Combined Cycle (I.G.C.C.) technology is considered the most favourable with electrical efficiency up to 40% [1]. Nevertheless, large bioenergy ventures have to face logistical problems to collect the required residual biomass fuel, different fuel feedstock around the yearly operation or the creation of energetic plantations with larger economic risk. Large Combined Heat and Power (CHP) units also have difficulties in selling heat to dedicated users in order to take full advantage of co-generation economics and are difficult to implement due to the complexity of the cooperation of the different stakeholders involved: biomass fuel producers, electricity, and heat consumers, power plant ownership, etc. High efficient smaller scale biomass CHP units could penetrate the market sooner than a greater consensus for larger biomass-to-power applications is achieved.

Small scale biomass CHP systems based on gasification can use internal combustion engines or micro gas turbines with electrical efficiencies from 20 to 30% of the biomass fuel lower heating value (LHV). Internal combustion engines offer higher electrical efficiency with reduced co-generation possibilities and

DOI of related article:10.1016/j.jpowsour.2005.11.040.
* Corresponding author. Tel.: +30 210 7723662/604; fax: +30 210 7723663.
E-mail address: ekak@central.ntua.gr (E. Kakaras).

0378-7753/$ – see front matter © 2006 Elsevier B.V. All rights reserved.
doi:10.1016/j.jpowsour.2005.12.024

Nomenclature

$A_{e,c}$	single heat pipe surface area in contact with fluidised bed (m^2)
A_i	constant used in Eq. (28) (Ω m)
$A_{INe,c}$	vapour/liquid interface surface in a heat pipe (m^2)
B_i	constant used in Eq. (28) (K)
b	parameter evaluated in Eq. (12)
D_i	parameter for Eqs. (31) and (32) ($A\,m^{-2}$)
D_{in}	internal heat pipe diameter (m)
D_{out}	external heat pipe diameter (m)
D_w	heat pipe wick internal diameter (m)
$D_{eff,i}$	effective diffusion coefficient of component i inside SOFC porous electrode material ($m^2\,s^{-1}$)
$D_{i,K}$	Knudsen diffusion coefficient of component i inside SOFC porous electrode material ($m^2\,s^{-1}$)
$D_{i,mix}$	diffusion coefficient of component i in mixture ($m^2\,s^{-1}$)
E_i	electrochemical reaction activation energy ($J\,mol^{-1}$)
F	Faraday constant = $6.023 \times 10^{23} \times 1.602 \times 10^{-19}$ ($Cb\,mol^{-1}$)
f_f	fin factor for heat pipes
$h_{e,c}$	combined convective and radiative heat transfer coefficient of a surface immersed in fluidised bed ($W\,m^{-2}\,K^{-1}$)
H_2O_{stoic}	stoichiometric moles of H_2O required for the simplified gasification reaction
H_L	latent heat of vaporisation of heat pipe working fluid ($J\,kg^{-1}$)
I	SOFC current (A)
J	SOFC current density ($A\,m^{-2}$)
k	thermal conductivity ($W\,m^{-1}\,K^{-1}$)
$L_{e,c}$	heat pipe length immersed in a fluidised bed (m)
LHV	fuel low heating value ($kJ\,kg^{-1}$ for solids/MJ m_n^{-1} for gases)
l_i	SOFC component thickness (m)
m_i	parameter for Eqs. (32) and (33)
n_i	component i mol flow ($mol\,s^{-1}$)
n_{HP}	number of heat pipes required
P	pressure (bar)
P_V	vapour pressure of heat pipe working fluid (Pa)
P_i	partial pressure of component i at the outlet of SOFC (atm)
P^O	standard pressure = 1 (atm)
P_{SOFC}	direct current electric power produced from the SOFC (W)
P_{COMP}	air compressor power
Q_{req}	required heat rate for allothermal gasification (W)
q_{HP}	the thermal energy transferred across a heat pipe (W)
R_{1-9}	heat pipe thermal resistances ($K\,kW^{-1}$)
R_{ACT}	activation surface specific electric resistance for SOFC ($\Omega\,m^2$)
R_{OHM}	Ohmic electric resistance for SOFC (Ω)
R_g	ideal gas constant ($8.314\,J\,mol^{-1}\,K^{-1}$)
S_{SOFC}	SOFC surface (m^2)
S_i	SOFC component surface (m^2)
STBR	steam to biomass ratio (refers to gasification)
$STBR_{stoic}$	stoichiometric steam to biomass ratio based on simplified gasification reaction
STCR	steam to carbon ratio (refers to product gas)
T	temperature (K)
U_f	SOFC fuel utilisation factor
V_{OC}	open circuit SOFC voltage (V)
V_{OHM}	Ohmic SOFC voltage over potential (V)
V_{ACT}	activation SOFC voltage over potential (V)
V_{PO}	polarisation SOFC voltage over potential (V)
y_i^0	molar fraction of component i in SOFC

Subscripts

comb	combustion
gas	gasification
in	input
out	output

Greek letters

α	ratio of heat pipe fin surface to bare surface
$\varepsilon_{electrode}$	void fraction of porous electrode material
ε_w	heat pipe mesh wick solid fraction
η_{fin}	common fin efficiency
$\eta_{el,SOFC}$	SOFC stack electrical efficiency
$\eta_{el,CHP}$	CHP electrical efficiency
ρ_i	specific electrical resistance of SOFC component i (Ω m)
$\tau_{electrode}$	tortuosity of porous electrode material

also exhibit higher pollutant levels. More advanced proposed systems use high temperature molten carbonate salts or solid oxide fuel cells. In the near future, the first commercial SOFC systems will be around 1 MW_e size, and their integration with biomass gasification in small scale configurations has recently gained attention [2,3].

This work presents the feasibility of high efficient bioenergy SOFC-CHP system in the range up to 1 MW_e, using a novel allothermal steam gasification reactor. A biomass allothermal fluidised bed (FB) gasifier operates at around 1073 K and produces an almost nitrogen free, medium calorific value gas mixture, rich in H_2, CO, and CH_4, which are fuel species for SOFCs. The product gas contains a significant amount of water vapour, depending on the amount of steam used for gasification and on the biomass fuel moisture as well. Water vapour in the fuel gas is necessary to reform CH_4, shift CO towards H_2, and prevent carbon deposition on the catalytic SOFC anode surface. Prior to using the product gas into an SOFC several contaminants must be removed and additional steam might be required to raise the steam to carbon ratio (STCR) in the anode. In order to achieve adequate thermal integration, hot gas cleaning has to be pursued to avoid sensible heat and water vapour loss by condensation at lower temperatures.

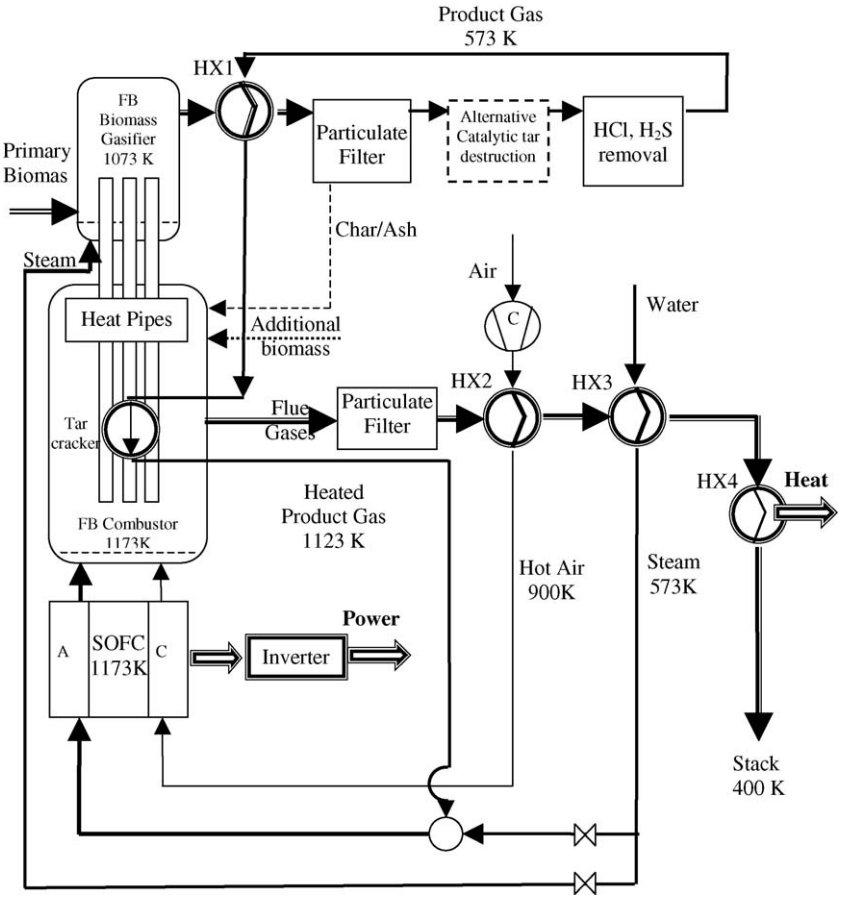

Fig. 1. Flowchart of the combined SOFC/allothermal biomass gasification CHP.

The main disadvantage of allothermal gasification processes is the requirement for external thermal energy input. In SOFCs, large amounts of rejected heat and depleted fuel necessitate large amounts of excess air mainly for cooling. The proposed system combines these two features into a useful outcome by thermally coupling a fluidised bed gasifier with a post fuel cell fluidised bed combustor. The combustion FB also utilises the gasifier by-product char as well as additional biomass if more heat is required. The total system operates at near atmospheric pressure.

The most common allothermal FB gasifier heat supply method is by means of hot bed material circulating between two fluidised beds one of which performs combustion [4,5]. The alternative thermal coupling of gasification and combustion FB with high temperature sodium heat pipes was the subject of the successful, recently completed EU-funded project "Biomass Heat Pipe Reformer" (BioHPR) [6].

To assess the proposed SOFC-CHP, a steady state model was built in Aspen Plus^{TM} process simulation software incorporating four subsections, namely: gasification, heat pipes, gas cleaning, and SOFC, analytically presented.

2. Total system configuration and modelling

The proposed CHP system flowchart consists of two fluidised bed reactors thermally coupled with heat pipes, a product gas cleaning train, a SOFC stack and its power conditioning, an air blower compressor, two gas-to-gas heat exchangers (HX1 and HX2), a heat recovery steam generator (HX3), and a hot water boiler (HX4) (Fig. 1). The gasifier and combustion FBs operate at 1073 K, ∼1.5 bar and 1173 K, ∼1.1 bar, respectively. This allows a 100 K temperature difference for heat transfer with the integrated sodium heat pipes to provide thermal energy requirements for the allothermal gasification. The raw product gas is cooled in HX1 to gas cleaning temperature requirements, particulates are removed by a barrier type filter and halogen and sulphide removal is accomplished in high temperature sorbent trap beds. The gas cleaning takes place at temperatures above tar dew point (see Section 5). The cleaned gas is reheated in HX1 and then enters a compact tar cracking reactor placed inside the combustion FB, where product gas temperature rises up to 1123 K. Additional steam is then added, increasing the gaseous fuel water content to avoid any carbon deposition on the SOFC anode. Air is blown to the near atmospheric pressure operating SOFC and is heated up to 900 K in HX2 before entering the stack. Depleted fuel and air from the SOFC are combusted in the secondary FB together with gasification by-product char. Additional biomass can be combusted if the above are not enough to sustain gasification. The flue gas thermal content is recuperated in HX2 followed by a heat recovery steam generator (HRSG) HX3, providing steam for the gasification and product gas moistening. Finally, HX4 offers useful thermal energy in the form of

hot water around 360 K. An inverter provides alternating current electrical power. The capacity of the system studied was based on an SOFC with 100 m^2 active surface resulting in electrical outputs of around 100–200 kW_e. This is a very commonly discussed and analysed SOFC size for various applications [7–9]. Nevertheless, the presented system is envisaged for up to 1 MW_e size and an attempt to present size independent data has been made.

The system was modelled in Aspen Plus™ 11 process simulation software. In all cases, the Redlich–Kwong–Soave cubic equation of state method was used for the properties estimation. Biomass was treated as non-conventional component. Existing unit operation models were combined with FORTRAN calculator blocks to model the performance of the four subsections. Pressure drops and thermal losses for each unit operation were assumed 2%. Heat exchangers were allowed a minimum $\Delta T = 100$ K in countercurrent mode. It was assumed that ambient air is at 293 K and 1.013 bar, the blower compressor isentropic efficiency is 0.7, while the electronic inverter efficiency is $n_{inv} = 95\%$.

3. Allothermal biomass gasification modelling and analysis

A simple and easy to adapt allothermal gasification model was built, to predict the main product gas composition including methane and char as well as the external heat required to drive the process.

3.1. Biomass allothermal gasification, description, and thermodynamics

The first step of biomass gasification is the immediate drying and thermal decomposition of solid fuel towards light gases, tars, and char. This step advances quickly in the high temperature and intense heat transfer environment of a fluidised bed. The pyrolysis gases and tars then react in the gas phase with the gasification agent, whereas solid char is participating in the heterogeneous reactions with gases. The main set of reactions is:

$$C_{(s)} + CO_2 \leftrightarrow 2CO \quad \text{Boudouard} \quad (1)$$

$$C_{(s)} + 2H_2 \leftrightarrow CH_4 \quad \text{Hydrogenating gasification} \quad (2)$$

$$C_{(s)} + H_2O \leftrightarrow CO + H_2 \quad \text{Heterogeneous water gas shift} \quad (3)$$

$$CH_4 + H_2O \leftrightarrow CO + 3H_2 \quad \text{Methane reforming} \quad (4)$$

$$CO + H_2O \leftrightarrow CO_2 + H_2 \quad \text{Water gas shift} \quad (5)$$

A simple way of approaching the biomass gasification modelling is by predicting thermodynamic equilibrium composition through Gibbs free energy minimisation calculations for the C, H, and O atoms of the fuel and the gasification agent mixture. The biomass ultimate analysis is given in Table 1 and corresponds to olive kernel residues. All thermodynamic properties (such as enthalpy of formation, etc.) can be derived from the higher heating value (HHV) [10].

Table 1
Biomass fuel data

Proximate analysis		Ultimate analysis (%w/w dry basis)	
Volatiles (%w/w dry)	72.64	C	51.19
Fixed carbon (%w/w dry)	24.78	H	6.06
Moisture (%w/w)	10.0	O	39.32
Heating values		N	0.76
HHV (kJ kg^{-1} dry)	18900	S	0.09
LHV (kJ kg^{-1} wet)	15567	Ash	2.58

A theoretical optimum of gasification operation is obtained when enough gasification agent is provided in order to fully convert all char to gaseous products according to equilibrium. Char is difficult to be modelled thermodynamically because of its complexity as a material. It is common to assume char as graphite, $C_{(s)}$, since it has well defined thermodynamic properties [11]. Fig. 2 shows the line of carbon boundary in a triangular C–H–O phase diagram, which was computed for the gasifier operating parameters $T_{gas} = 1073$ K, and $P_{gas} = 2$ bar. Above the solid carbon boundary, solid carbon is thermodynamically stable, while below it there is no carbon predicted. The biomass fuel composition lies in the heterogeneous region, therefore a gasification agent containing oxygen or/and hydrogen (in this work purely steam) must be added to drive the equilibrium towards complete conversion of char into gaseous fuel species for the SOFC. It is common to express the extent of steam addition as steam to biomass ratio (STBR):

$$\text{STBR} = \frac{\dot{\text{Steam}} + \text{Fuel moisture}\,(\text{kg s}^{-1})}{\text{Dry biomass}\,(\text{kg s}^{-1})} \quad (6)$$

Thermodynamics predict that the minimum value for steam to biomass ratio must be $\text{STBR}_{min} \approx 0.4$, in order to secure complete fuel carbon conversion into gaseous compounds for the given pressure, temperature, and biomass fuel composition.

An alternative expression to the STBR is the *excess stoichiometric steam* [12] based on a simplified gasification reaction in

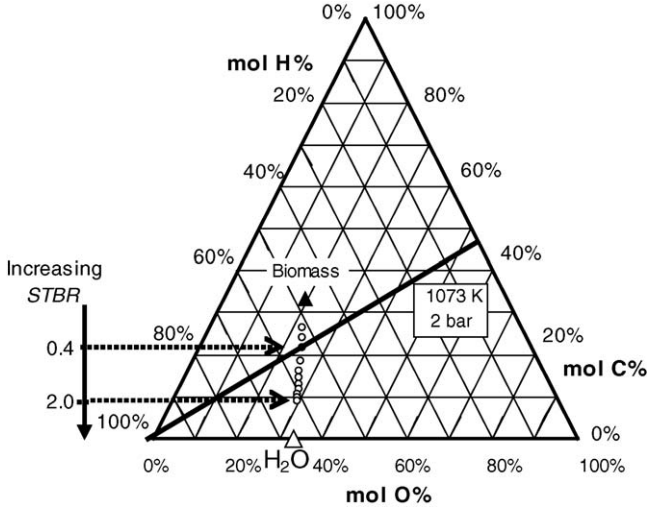

Fig. 2. Various STBR locations on a ternary C–H–O diagram with carbon boundary line at $T_{gas} = 1073$ K and $P_{gas} = 2$ bar.

the form of:

$$CH_nO_m + (1-m)H_2O \leftrightarrow \left(\frac{n}{2} + 1 - m\right) H_2 + CO \quad (7)$$

For the fuel considered, $n = 0.16$ and $m = 0.77$. The stoichiometric steam to biomass ratio is expressed:

$$STBR_{stoic} = \frac{\tilde{M}_{H_2O,stoic}}{\tilde{M}_{biomass}} = \frac{(1-m)18}{12 + n + 16m} \quad (8)$$

where $\tilde{M}_i$ are the mass flows of steam and biomass. Therefore, for reaction (7), $H_2O_{stoic} = 0.24$ mol for 1 mol of biomass, and from reaction (8), $STBR_{stoic} \approx 0.2$. Dividing the actual STBR values with $STBR_{stoic}$ gives the excess steam.

Kinetics of biomass gasification at 973–1173 K and realistic residence times allow higher concentrations of CH_4 and other hydrocarbons to be present in the gasifier outlet, in contrast to what thermodynamics predict [13]. Char might also "escape" the reactor before reacting completely even though the condition $STBR > STBR_{min}$ is valid. Unstable thermodynamically constituents actually appear during an actual gasification process, the derivation of which can be attributed to partial reactions among the products of the initial decomposition step. Therefore, a more accurate model should be build by accommodating non-thermodynamic corrections for these products.

3.2. Gasifier model based on thermodynamics with non-ideal corrections

The gasification Aspen Plus™ modelling subsection is shown in Fig. 3. The heat streams (dashed lines), representing enthalpy differences between inputs and outputs of each reactor model block, are added to form the thermal energy requirement stream. In the first step (RYIELD), the biomass material is transformed from a non-conventional solid into its elements. This is common practice when dealing with solid fuel materials in Aspen Plus™. The non-equilibrium char amount is directly split towards the syngas outlet. Similar approach models use a ratio of 15% non-equilibrium char for circulating fluidised bed allothermal gasification [14]. A somehow lesser value was adopted, i.e. 10%, as more appropriate for a bubbling fluidised bed having longer residence times. The rest of the elemental composition is fed to the (RSTOIC) reactor where CH_4 and tar are formed. The extent of methane formation was set to use 10% of the elemental carbon in the biomass fuel. This allows methane concentrations in the gasification subsection outlet to range from 5 to 10% (v/v) which are in agreement with commonly measured values. In order to avoid having a large variety of tar compounds, this group is represented only by naphthalene, which is a major tar component in biomass gasification processes. The amount of tar was specified to allow ~1–5 g m_n^{-3} in dry basis product gas, according to literature about steam gasification experiments with catalytic in situ FB tar reduction [15]. The remaining elemental biomass and steam are fed to an (RGIBBS) reactor model where according to Gibbs free energy minimisation calculations (for the specified temperature and pressure), the equilibrium composition is evaluated, considering the components CH_4, CO, CO_2, H_2, H_2O, and $C_{(s)}$. The equilibrium outlet is mixed with hydrocarbons and char slip streams to form the final syngas outlet stream. The effect of the correction of slip streams for carbon conversion and methane in product gas content, in comparison to thermodynamic predictions is illustrated in Fig. 4.

The model was run for different STBR at 1073 K and 2 bar (Fig. 5). Since part of the fuel carbon is not participating in the equilibrium, the discontinuity of composition lines signifying the total carbon conversion ($STBR_{min}$) appears at a slightly lower value compared to pure thermodynamics prediction. The lower heating value (LHV) of the humid and dry gas is reduced with increased STBR. Heat, Q_{req}, to sustain gasification at T_{gas}, increases with STBR (Fig. 6). The amount of steam relative to the carbon containing species is defined as steam to carbon ratio (STCR). A desired value $STCR > 2$ is set to avoid any carbon deposition on SOFCs (see Section 6.1). Fig. 6 also shows that

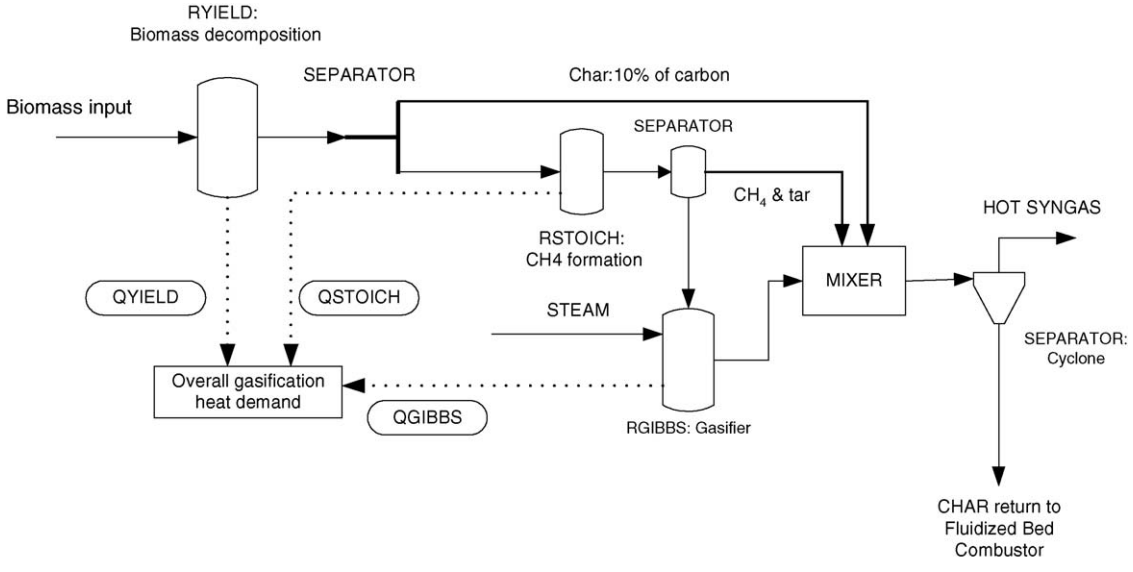

Fig. 3. Aspen Plus™ biomass gasification modelling flow sheet.

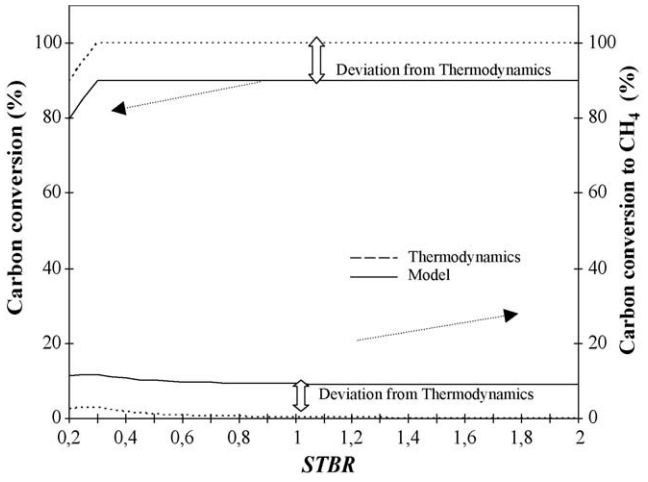

Fig. 4. Comparison of model and thermodynamic equilibrium prediction for carbon conversion and methane production.

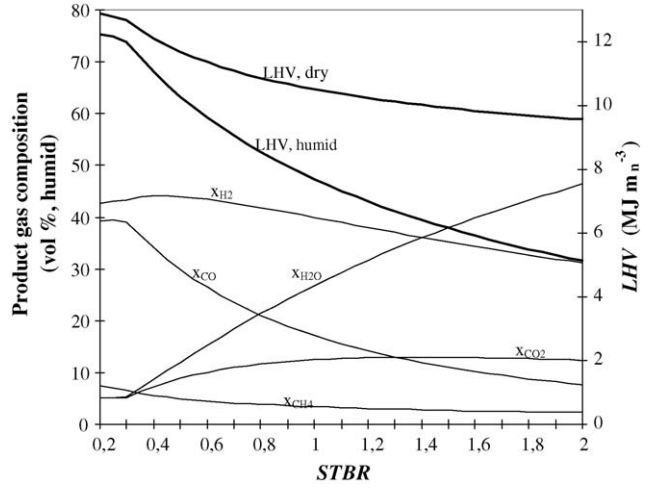

Fig. 5. STBR effect on wet basis product gas composition and LHV at $T_{gas} = 1073$ K and $P_{gas} = 2$ bar.

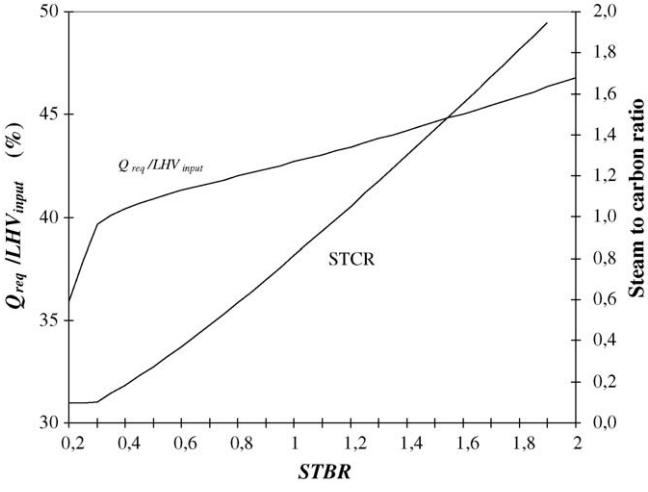

Fig. 6. STBR effect on Q_{req} for gasification and resulting STCR at $T_{gas} = 1073$ K and $P_{gas} = 2$ bar.

this can be achieved from the gasification step using STBR > 2, instead of having to add steam at a latter stage.

For the total system operation a relatively low STBR = 0.6 was chosen for maximising carbon conversion without excessive heat demands. Kinetic reasons such as pushing towards completion of tar reforming reactions, or fluidisation limitations might pose higher STBR in practice.

4. Heat pipes modelling and analysis

4.1. Heat pipe description

Heat pipes are simple and effective heat transfer equipment without moving parts taking advantage of the large latent heat of vaporisation of a working fluid that returns from the condenser to the evaporator by capillary action. A simple heat pipe is a hollow tube with some layers of wire screen along the inner wall to serve as wick (Fig. 7). The wick is filled with a wetting liquid having a boiling point near the desired application temperature. Sodium heat pipes have a useful range of heat transfer applicability from 870 to 1470 K [16], and have been used successfully for the BioHPR reactor thermal coupling of two fluidised beds performing endothermic biomass gasification and exothermic combustion [6].

4.2. Modelling of heat pipes

A single heat pipe model was made in a FORTRAN calculator block in Aspen Plus™, to estimate its total thermal resistance, temperature drop, and heat transfer rate. The number of heat pipes required was then calculated according to the total Q_{req}.

A single heat pipe heat transfer model comprises of nine thermal resistances R_1–R_9 (Fig. 7). R_1 and R_9 are external convection resistances of the evaporator and condenser section. The heat pipe external surfaces can incorporate fins enhancing heat tranfer. If α is the ratio of fin surface to bare (i.e. no-fins) tube surface, i.e. $\alpha = A_{fin}/A_{e,c}$, and a fin factor is defined as $f_f = (1 + \eta_{fin}\alpha)$, with η_{fin} the commonly used fin efficiency, both R_1 and R_9 can be expressed as:

$$R_{1,9} = \frac{1}{f_f h_{e,c} A_{e,c}} \tag{9}$$

where $h_{e,c}$ (W m^{-2} K^{-1}) is the combined convective and radiative heat transfer coefficient of a surface immersed in fluidised bed, and $A_{e,c} = \pi D_{out} L_{e,c}$ in (m^2) is the outer surface of the bare heat pipe tube. The fin factor is introduced to enable a more generic presentation of results rather that going into detailed calculations for different fin types. A value of $f_f = 2$ is assumed throughout the calculations. There are numerous experimental studies which derive correlations for heat transfer coefficients in fluidised beds, unfortunately not generic because of the complex nature of fluidisation contacting [17]. The arrangement of the heat pipes, the fluidisation velocity, the bed inventory material characteristics, etc., are some of the parameters that influence the final value for h. Table 2 summarises the assumptions for h by averaging values reported in literature [17–19]. The evaporator

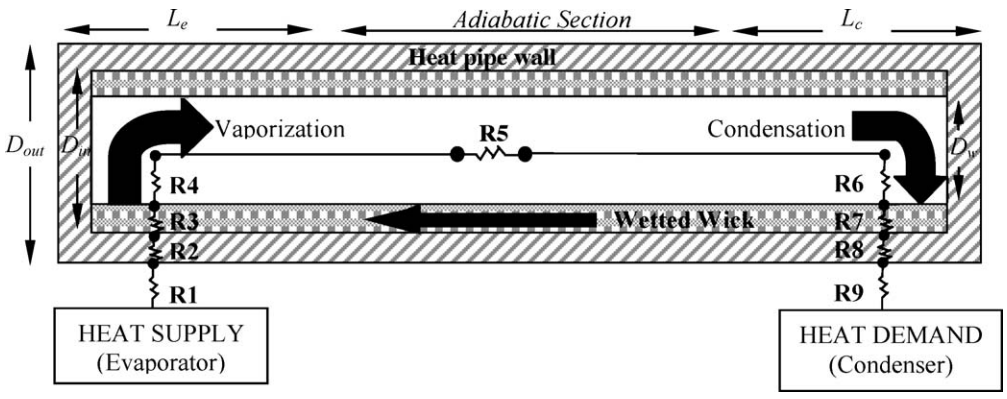

Fig. 7. Heat pipe operating principle and thermal model.

Table 2
Assumptions for the external heat transfer coefficient of heat pipes

Heat transfer coefficient (heat pipe section)	Conditions for the assumption ($W\,m^{-2}\,K^{-1}$)	
h_e (evaporator section)	300 (combustion FB) [17–19]	50 (flow inside SOFC) [21]
h_c (condenser section)	300 (gasification FB) [17–19]	

section could alternatively be placed inside a usual post-SOFC combustor. The practical applicability of this is also examined but using a smaller value of h [20].

Resistances R_2 and R_8 represent conduction through the heat pipe tube material. Since a cylindrical heat pipe is assumed these resistances are in the form of:

$$R_{2,8} = \frac{\ln(D_{out}/D_{in})}{2\pi k_m L_{e,c}} \tag{10}$$

where k_m is the thermal conductivity of the heat pipe shell in ($W\,m^{-1}\,K^{-1}$).

Similarly, the thermal resistances R_3 and R_7 through the wick are:

$$R_{3,7} = \frac{\ln(D_{in}/D_w)}{2\pi k_w L_{e,c}} \tag{11}$$

The evaluation of the combined solid and liquid thermal conductivity of a wetted mesh wick was accomplished using the following set of expressions from [16]:

$$k_w = \left(\frac{b-\varepsilon_w}{b+\varepsilon_w}\right) k_l \tag{12}$$

where ε_w is the solid fraction of the mesh wick, and

$$b = \frac{1+(k_s/k_l)}{1-(k_s/k_l)} \tag{13}$$

where k_l and k_s are the thermal conductivities of the liquid working fluid and the wick solid material, respectively.

R_4 and R_6 correspond to the liquid/vapour interface resistance to heat transfer and are given in the form of [16]:

$$R_{4,6} = \frac{R_g T^2 (2\pi R_g T)^{1/2}}{H_L P_v A_{INe,c}} \tag{14}$$

where $A_{INe,c} = \pi D_w L_{e,c}$ is the surface of the vapour liquid interface, R_g the ideal gas constant, H_L the latent heat of vaporisation of the working fluid in ($J\,kg^{-1}$), and P_V is the vapour pressure of the working fluid in (Pa).

Finally, R_5 is the resistance due to temperature drop along the vapour transferred from the evaporator to the condenser. This is usually the smallest resistance and could be evaluated from:

$$R_5 = \frac{R_g T^2\,\Delta P_V}{q_{HP} H_L P_V} \tag{15}$$

where q_{HP} (W) is the thermal energy transferred across the heat pipe and ΔP_V is the vapour flow pressure drop in (Pa). Nevertheless, expression (15) was omitted and R_5 was assumed to be negligible. Otherwise its estimation would require a more complex iterative process to converge, as it involves q_{HP}, which is essentially the outcome of the heat pipe model. An iterative loop for the convergence of the sodium vapour temperature already exists.

The heat transfer rate of a single heat pipe is:

$$q_{HP} = \frac{\Delta T}{R_{tot}} = \frac{T_{comb} - T_{gas}}{\sum_{i=1}^{9} R_i} \tag{16}$$

where T_{comb} and T_{gas} are combustion and gasification FB temperatures, respectively. The number of heat pipes is then evaluated as $n_{HP} = Q_{req}/q_{HP}$. The assumptions for the physical dimensions of a single heat pipe are given in Table 3 and the necessary thermophysical property estimations in Table 4 based on [21,22].

Table 3
Assumptions and dimensions for a single heat pipe

Physical heat pipe dimensions
$D_{out} = 0.03$ m, $D_{in} = 0.025$ m, $D_w = 0.00242$ m, $L_e = L_c = 1$ m, $\varepsilon_w = 0.415$

Table 4
Thermo physical properties of the single heat pipe thermal model

Thermo physical properties	Units	Ref.
$k_m = k_s = 27$	($W\,m^{-1}\,K^{-1}$)	[21]
$k_l = 124.67 - 0.11381T + 5.5226 \times 10^{-5}T^2 - 1.1842 \times 10^{-8}T^3$	($W\,m^{-1}\,K^{-1}$)	[22]
$H_L = 393.97(1 - (T/T_C)) + 4398.6(1 - (T/T_C))^{0.29302}$	($kJ\,kg^{-1}$)	[22]
$\ln P_V = 11.9463 - 12633.73/T - 0.4672 \ln T$	(MPa)	[22]
Where T = sodium operating temperature (K), and $T_C = 2503.7$	(K)	[22]

Table 5
Heat transfer model results for a single heat pipe between two fluidised beds at 1073 and 1173 K

Thermal resistances ($K\,kW^{-1}$)									
R_1	R_2	R_3	R_4	R_5	R_6	R_7	R_8	R_9	R_{tot}
17.69	1.075	0.157	3.1E−5	0	3.1E−5	0.157	1.075	17.69	37.843

Vapour sodium temperature (K)	Sodium vapour pressure (bar)	Heat transfer rate (kW/heat pipe)
1123	0.75	2.642

The results for the single heat pipe modelling between two fluidised beds are summarised in Table 5. Most of the heat transfer resistance originates from external heat pipe convection. The number of heat pipes required to sustain gasification per 1 MW_{LHV} biomass input into the gasifier is shown in Fig. 8 for varying STBR for two cases: (a) thermal coupling of gasification and combustion FBs and (b) gasification FB coupled with a typical SOFC stack afterburner. Due to increased evaporator external resistance, the latter requires approximately four times the number of heat pipes creating however additional problems; it would be difficult to fit them in the FB gasifier as well as into a SOFC system, capital costs associated with heat pipes would be quadrupled, and consequently, a totally new stack design would be required. For the above reasons the present work examined only the formal thermal coupling. The required number of heat pipes between two FBs is also graphed for another two ΔTs. Gasification at lower temperatures would result in excessive tar content and combustion above 1173 K could potentially create problems of bed material and ash agglomeration, since all ash removed from the raw product gas passes through the combustor

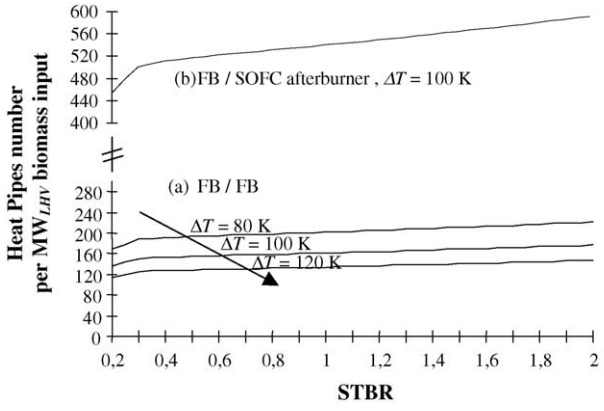

Fig. 8. Number of heat pipes required per MW_{LHV} fuel input in the gasifier vs. STBR used when heat derives from: (a) a secondary FB at various ΔTs (b) an SOFC post combustor.

at very high temperature. For design point of $\Delta T = 100$ K, 180 heat pipes per MW_{LHV} gasifier fuel input is chosen to satisfy the gasification for STBR up to 2, if required.

5. Gas cleaning analysis

5.1. Product gas impurities and SOFC fuel specification

The hot product gas at the outlet of the gasifier FB contains a number of trace impurities that can be harmful for fuel cells:

- *Particulates*: Which are mainly un-reacted char, biomass fuel ash, and FB inventory material.
- *Alkalis*: Part of the alkali content in the fuel ash can appear in the gas phase of the product in the form of thermodynamically favourable volatile compounds at high temperatures [23].
- *Ammonia*: Most of the biomass fuel-bound nitrogen is usually emitted during the pyrolysis step as ammonia. Despite ammonia being an unstable molecule, in gasification conditions its subsequent decomposition is slow [24].
- *Sulphur and halogens*: In gasification processes, fuel sulphur is stable in the form of hydrogen sulphide and to a lesser extent carbonyl sulphide especially in case of increased water content because of the equilibrium:

$$COS + H_2O \leftrightarrow H_2S + CO_2 \quad (17)$$

H_2S concentrations in product gas could range from 20 to 500 ppm [25,26], and therefore cause problems to fuel cells. Halides appear mainly as HCl. Some biomass fuels, such as straw, have significant amounts of chlorine content that should be avoided for gasification applications with fuel cells. Apart from their elemental concentration in the biomass feedstock, the sulphur and halide concentration levels in the product gas also depend on the gasifier conditions, and the relative proportions of ash metal components tending to form stable solids with them [27].

Table 6
Fuel impurity tolerances for SOFC

Impurity	Upper limit	Comments	Ref.
Particulates (ppmw)	0.1	–	[31]
NH_3 (ppmv)	5000	–	[31,32]
H_2S (ppmv)	3000	Operation above 1273 K	[32]
	1	Non-permanent poisoning	[32]
	0.1	Commercial target	[31]
Halides (ppmv)	1	–	[31,32]
Alkali vapours	–	Not available data found	–
Tar compounds	–	Not available data found	–

- *Tar*: A major group of product gas impurities, is a complex mixture of organic compounds generally assumed aromatic, produced during biomass gasification [28]. Estimates of the tar dew point on presently identified species show that tars condense at temperatures below 473 K [29]. To be on the safe side and to account for heavier tar species a higher temperature of 523 K was adopted. When condensed, tars form persistent aerosols, the combustion or exposure to high temperatures of which leads to soot formation and coking of surfaces. Furthermore, condensed tars are extremely sticky and cause blocking and fouling of equipment downstream.

The tolerance of different power production technologies to these impurities vary from internal combustion engines being the most resistant, followed by gas turbines and fuel cells; presently having the most stringent fuel specifications. High temperature fuel cells, such as SOFCs, are more impurity resistant compared to low temperature ones [30]. Table 6 summarises reported fuel impurity tolerances for SOFCs [31,32]. The most well documented impurity is H_2S which poisons the anode nickel-based catalytic surface of SOFCs. The more stringent level of 0.1 ppm H_2S reported as a target for product gas purification [31] best represents a commercial type application for thousands of hours of trouble free operation. The implications of the other biomass derived product gas impurities on SOFCs are scarcely documented since this subject has only recently been the focus of experimental efforts. Vapour alkali compounds as well as other volatile metals, such as zinc, are very drastic and are able to attack the catalytic surface of SOFCs. These can either be introduced into the gas during the gasification step or during hot gas cleaning process involving sorbents containing these elements. Special care has to be given to the silicon purity level because it is usually a main component of biomass ash and FB inventory. Silicon can be deposited on the anode as silica (SiO_2) and the transport is enhanced throughout the cell by high (~50%) H_2O content in the fuel according to the following reaction [32]:

$$SiO_{2(S)} + 2H_2O_{(g)} \rightarrow Si(OH)_4 \quad (18)$$

Partial decomposition of tar compounds can occur at the high water vapour content and high temperature anode environment, but in case of remaining tar, carbon deposition could occur. Therefore, tar should be eliminated to the maximum possible extent.

5.2. Gas cleaning and conditioning scheme

A hot gas cleaning process is examined in order to avoid great losses of useful heat due to water vapour condensation and product gas sensible heat loss during excessive cooling.

Tars can be reduced by using natural or synthetic catalytic gasification FB inventory materials [33]. If cleaning the gas from other contaminants requires temperatures below the remaining tar dew temperature, then complete tar elimination should take place immediately after the gasifier, while the gas is still hot. This is usually accomplished in a catalytic cracking reactor. Catalytic particulate filters could also be employed for combined tar and particulate removal [25]. Assuming that downstream gas cleaning process conditions assure no tar condensation, the catalytic eliminator could also be placed at the final stage of heating the product gas prior to the SOFC. Adequate tar cracking temperatures can be achieved within the hot flue gas stream of the combustion FB (Fig. 1). Tar cracking at the latter stage prior to the SOFC will increase the catalyst life (usually nickel based [34]) by exposing it to minimum poisonous hydrogen sulphide. If no initial tar cracker is required it would allow the raw product gas to be cooled down to a lower level and the barrier type filter could be manufactured of less costly material.

At such temperature levels ($T < 800$ K) all of the alkali content will be in the solid phase condensed on particulates that are filtered out. Part of the alkali removed will probably drag down some of the halide content. The remaining gaseous halide compounds (mainly HCl) can be removed by a dry sorbent bed containing sodium, in form of Na_2CO_3 which is a rather cheap, naturally occurring material [31]:

$$Na_2CO_3 + 2HCl \leftrightarrow 2NaCl + CO_2 + H_2O \quad (19)$$

For hydrogen sulphide removal, several metal oxides have been extensively examined in the past decade for desulphurisation of high sulphur coal derived gas in regenerative mode so as to avoid excessive sorbent material costs and allow sulphur recovery in valuable by-product forms (i.e. elemental or sulphuric acid) [35–37]. For smaller scale (up to 10 MW_e) biomass power applications the advantage of recovering sulphur would be negligible, due to the prohibiting capital costs of regenerative desulphurisation and the relatively low sulphur content of biomass. Therefore, biomass fuels with low sulphur content must be preferred, while for eliminating small concentrations of H_2S a hot non-regenerative sulphur scavenging process is used based on zinc oxide (ZnO) sorbent. Zinc has a great affinity with sulphur and is fairly reduction resistant at temperatures up to 810 K with limited Zn losses by boil-off [37]. Desulphurisation is achieved through the following reaction:

$$ZnO_{(s)} + H_2S = ZnS_{(s)} + H_2O \quad (20)$$

Zinc oxide sorbents are commercially available as cylindrical extrudates [38] and can be used to form a fixed bed sulphur trap. Such systems used in hydrocarbon processing are usually designed to last for months of operation. It has to be noted that HCl removal has to precede that of H_2S to avoid possible interaction of HCl with the ZnO [37].

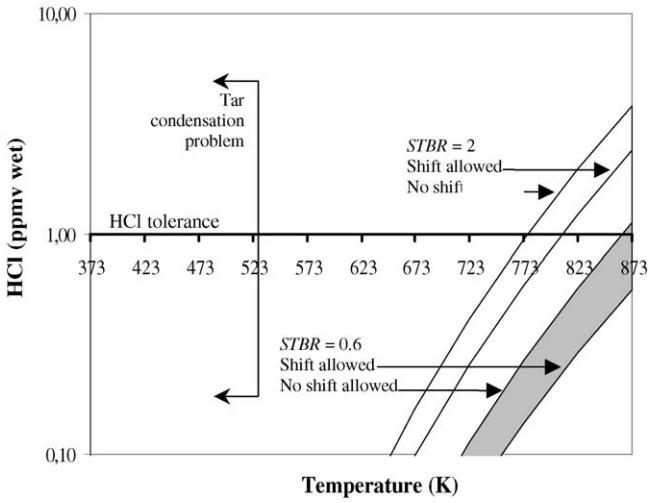

Fig. 9. Thermodynamic prediction of HCl concentration escaping a Na_2CO_3 bed vs. temperature, for different STBR, *with* and without shift reaction into account.

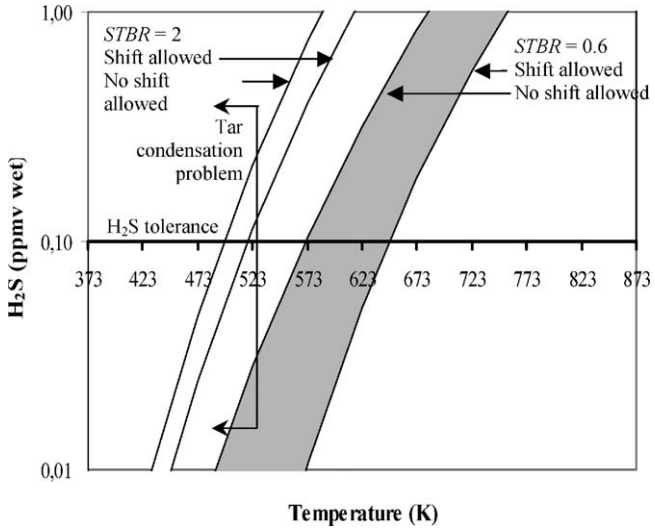

Fig. 10. Thermodynamic prediction of H_2S concentration escaping a ZnO bed vs. temperature, for different STBR, *with* and without shift reaction into account.

During the operation of HCl and H_2S trap beds three zones can be identified: the reacted sorbent, the reaction head and the un-reacted sorbent zone. Equilibrium of reactions (19) and (20) is closely approached at high temperatures, and reaction constants expressions can be a good approximation for predicting the product gas outlet concentration [38]:

$$K_p = \frac{P_{H_2O} P_{CO_2}}{P_{HCl}} \quad (21)$$

$$K_p = \frac{P_{H_2O}}{P_{H_2S}} \quad (22)$$

Due to chemisorption of H_2S on ZnO, the actual H_2S level at the exit of the bed can be even lower than Eq. (22) predicts [39].

Equilibrium calculations were performed with an Aspen Plus^{TM} (REQUIL) reactor model assuming an initial value of 100 ppmv HCl and 100 ppmv H_2S and sorbent double of the stoichiometric required (the latter has no effect as solid materials do not participate in the chemical equilibrium constant evaluation). The gas cleaning is more efficient at lower water vapour content (i.e. lower STBR used in the gasifier) and lower temperatures. In comparison with results for gas cleaning of air gasification products [40], where water vapour fraction is less, the removal of contaminants from steam gasification requires lower temperatures to achieve the same degree of purification. The upper and lower effect of water vapour on predicted outlet contaminant concentrations because of shift reaction reaching equilibrium or not is taken into account by presented results for both cases. Concentrations of 1 ppm HCl can be achieved at 773 K even for large excess water vapour content (Fig. 9). On the other hand, cleaning the gas to less than 0.1 ppm H_2S requires temperatures about 573 K for the low STBR = 0.6 (Fig. 10) and tar condensation can be avoided. For STBR = 2 cleaning must be done at less than 523 K, which means some heavier tar condensation might occur. Apart from relieving the heat pipe requirement to deliver heat to gasification, more effective H_2S cleaning is another reason for choosing low STBR.

6. SOFC configuration, modelling, and analysis

6.1. SOFC configuration

A typical tubular cathode supported SOFC similar to the Siemens Westinghouse system is examined for the integrated system. A high SOFC operating temperature is typically chosen $T_{SOFC} = 1173$ K in order to satisfy gasification heat demand. Alternative SOFC configurations and materials with more detailed modelling will be presented in a future paper. Having in mind that the product gas tar burden might not be 100% eliminated, and that carbon deposition will have to be avoided within the anode, it is possible that lower operating temperature SOFCs with alternative coking resistant catalytic materials might be more appropriate [41].

The SOFC system layout differs in some aspects from the usual configurations for applications based on natural gas: both anode and cathode depleted fuel and air are introduced to the secondary FB combustor. The operating pressure is chosen at $P_{SOFC} \cong 1.5$ bar, enough to overcome combustion FB, flue gas cleaning, and subsequent heat recovery exchanger pressure drops. The input fuel gas is expected to contain very little amounts of methane or other hydrocarbons since a heavy hydrocarbon-eliminating reactor is used. Therefore, the common internal pre-reformer for methane [20] is not used here. Furthermore, there is no recirculation of anode depleted gases rich in water vapour, as commonly proposed for natural gas fuelled SOFCs [7], and supplementary steam has to be supplied to the cell to ensure carbon deposition free operation. A recirculation loop based on ejectors would require excessive product gas pressures to drive this process. The additional quantity of steam is specified to achieve a steam to carbon ratio (STCR), of at least 2:

$$\text{STCR} = \frac{n_{H_2O}}{n_{CH_4} + n_{CO} + n_{CO_2}} \quad (23)$$

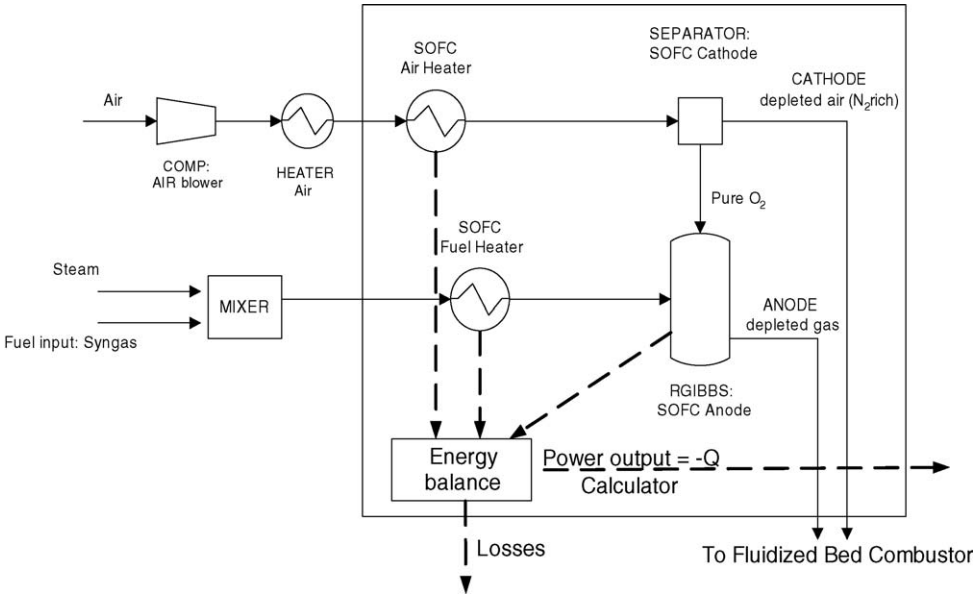

Fig. 11. Aspen Plus™ SOFC modelling flow sheet.

where n_i are the flow rates (mol s^{-1}) of H_2O, CH_4, CO, and CO_2 entering the anode. Similar or slightly higher STCR values are used when partially pre-reformed methane is fed to SOFCs to assure no carbon deposition will occur [7,8].

Moistened fuel and air are supplied to the cell at ~1073 and 900 K, respectively. Air can be internally heated up closely to the operating temperature before reaching the cathode material. In this work, the heat for bringing air closer to cathode temperature (from 900 towards 1173 K) is not supplied by the post combustor—which is a common practice in natural gas SOFC cycles [7,8]. The post combustor available heat is solely used to drive gasification; therefore air temperature rise must be accomplished within the SOFC stack from the dissipated heat.

6.2. SOFC modelling

A simple SOFC model was built in Aspen Plus™ using available blocks and a FORTRAN calculator (Fig. 11). Incoming air and fuel are brought to SOFC operating temperature with (HEATER) blocks. The electrochemically reacted oxygen is separated in the cathode, modelled by a (SEPARATOR) block, and fed to the anode, modelled by an (RGIBBS) reactor model, bringing the anode mixture into chemical equilibrium. The inlet low methane content justifies this equilibrium assumption rather than using available methane reforming rate reactions [42]. The main parameter used in the modelling is the fuel utilisation factor U_f, expressed as:

$$U_f = \frac{n_{H_2,REACT}}{n_{H_2,in} + n_{CO,in} + 4 \cdot n_{CH_4,in}} \quad (24)$$

where $n_{H_2,REACT}$ is the H_2 (mol s^{-1}) reacting in the electrochemical reaction (23) and $n_{i,in}$ refers to the anode's fuel species input. For achieving a desired U_f the amount of oxygen passing through the cathode is specified as $n_{O_2,REACT} = 0.5(n_{H_2,REACT})$. The model is run for $U_f = 0.55$–0.85, typical values for SOFC operations.

A total active cell surface $S_{SOFC} = 100\,m^2$ is used for all calculations. The electrical power output from the SOFC stack is calculated in a FORTRAN block and participates in the overall energy balance MIXER as a negative heat stream representing energy driven out of the cell. The total air supply for the cell is calculated so as to achieve thermal losses of 5% of the initial SOFC thermal input.

The FORTRAN block estimating the SOFC electrochemical parameters is based on literature models from Chan et al. [43,9], Costamagna et al. [7], Campanari and Iora [44], and Selimovic [45]. Only the electrochemical oxidation of hydrogen is considered:

$$H_2 + (1/2)O_2 \leftrightarrow H_2O \quad (25)$$

based on the assumption that the electrochemical oxidation of CO and CH_4 is much slower than the shift and reforming reactions producing H_2 which can react faster through reaction (25) [32]. The Nernst open circuit cell voltage V_{OC} at T_{SOFC}, which is an average temperature between the mixed anode and cathode inlet flow, at approximately 950 K and the outlet of the SOFC, at 1173 K, is:

$$V_{OC} = -\frac{\Delta G^\circ}{2 \cdot F} + \frac{R_g \cdot T_{SOFC}}{2 \cdot F} \ln \frac{P_{H_2}^{out} (P_{O_2}^{out})^{1/2}}{P_{H_2O}^{out}} \quad (26)$$

where $F = 6.023 \times 10^{23} \times 1.602 \times 10^{-19}\,C\,mol^{-1}$ is the Faraday constant, 2 is the number of e^- produced per H_2 mole that reacts through reaction (25) which has a molar Gibbs free energy change of $\Delta G^\circ = \Delta H^\circ - T_{SOFC}\,\Delta S^\circ$, calculated at T_{SOFC} and at standard pressure, and finally, P_i^{out} are the partial pressures of the participating components in reaction (25) considered as the average values of the inlet and outlet gas streams in and out of the anode and cathode. The assumption of average temperature and gas composition between SOFC inlet and outlet is compared

Table 7
Equations and constants for evaluation of SOFC Ohmic resistances

Equations used	Component resistance : $R_i = \rho_i \frac{l_i}{S_i}\ (\Omega)$	(27)
	where l_i is the current flow length, S_i is the area through which the current flows, calculated according to [44]	
	Specific resistivity : $\rho_i = A_i \cdot e^{-(B_i/T_{OP})}\ (\Omega\,m)$	(28)
	Total resistance : $R_{OHM} = R_{el} + R_a + R_c + R_{int}\ (\Omega)$	(29)

Component [9]	Material	A_i (Ω m) $\times 10^6$	B_i (K)
Electrolyte	YSZ	2.94	−10350
Anode	Ni/YSZ	2.98	1392
Cathode	LSM-YSZ	8.114	−600
Inter-cell connector	Doped $LaCrO_3$	1256	−4690

against detailed estimation of fuel parameters in [46]. The ideal cell voltage is reduced by Ohmic, activation, and concentration losses or overpotentials all of which are taken into account as follows:

a. Table 7 gives a short description of the evaluation of Ohmic resistances due to limited electrical conductivity of anode, cathode, and inter-cell connection points as well as ionic conductivity limitations of the electrolyte. For the tubular configuration assumed, the tube dimensions and the current path flows are considered, taking into account the circumferential current flows in the anode and cathode, according to Campanari and Iora [44]. The Ohmic voltage losses are evaluated as: $V_{OHM} = R_{OHM} I$ (V), where I (A) the total cell stack current given by:

$$I = 2Fn_{H_2,REACT} \tag{30}$$

The Ohmic voltage loss calculated is in the range 80–120 mV, depending on the SOFC operating parameters, which agrees with values given in literature [47].

b. Activation polarisation losses occur due to slow electron release or capture steps in the electrode–electrolyte bilayer and are evaluated as surface specific Ohmic resistances, R_{ACT} in ($\Omega\,m^2$) (Table 8). The activation voltage losses are evaluated as $V_{ACT} = (R_{ACT} J)$ (V), where J is the current density (A m^{-2}):

$$J = \frac{I}{S_{SOFC}} \tag{34}$$

c. Concentration polarisation losses are caused by limited diffusion of gaseous reactants and products species in and out of reaction sites inside the porous SOFC electrodes. Usually concentration losses are small unless very large oxygen or fuel utilisations are reached. It was decided at an early stage to include their estimation because of the particularity of the proposed system: the absence of a post combustor in the stack results in lower air demands for cooling and thus greater air utilisation that could potentially reach near SOFC oxygen starvation. In that case the concentration overpotentials could have been significant. However, such high oxygen utilisations were not observed in the final calculations presented. The concentration polarisation voltage losses are estimated in voltage drop terms by expressing the relative concentration difference of species participating in (25) on reaction sites and bulk SOFC flow. This reduction is controlled by Fick's law of diffusion inside the electrode pores. The final forms of equations are given in Table 9 together with the assumptions for the evaluation of the effective combined ordinary and Knudsen diffusion coefficients. The analysis is based on Selimovic [45].

According to the simulation model the output voltage of the cell is:

$$V = V_{OC} - V_{OHM} - V_{ACT} - V_{PO} \tag{39}$$

The cell power output is:

$$P_{SOFC} = V \cdot I \tag{40}$$

Table 8
Equations and constants for evaluation of SOFC activation resistances

Equations used	Anode: $\frac{1}{R_{ACT\_A}} = D_1 \cdot \frac{2 \cdot F}{R_g \cdot T_{SOFC}} \cdot \left(\frac{P_{H_2}}{P^O}\right)^{m1} \cdot e^{-(E_A/R_g \cdot T_{SOFC})}\ (\Omega^{-1}\,m^2)$ (31)			
	Cathode: $\frac{1}{R_{ACT\_C}} = D_2 \cdot \frac{4 \cdot F}{R_g \cdot T_{SOFC}} \cdot \left(\frac{P_{O_2}}{P^O}\right)^{m2} \cdot e^{-(E_C/R_g \cdot T_{SOFC})}\ (\Omega^{-1}\,m^2)$ (32)			
	Total activation surface specific resistance: $R_{ACT} = R_{ACT\_A} + R_{ACT\_C}\ (\Omega^{-1}\,m^2)$ (33)			
Electrode properties [7]	D_i (A m^{-2})	m_i	P^O (atm)	E_i (J mol^{-1})
Anode	2.13×10^8	0.25	1	110000
Cathode	1.49×10^8	0.25	1	110000

Table 9
Equations and constants for evaluation of SOFC concentration overpotential

Equations used	Anode overpotential: $V_{\mathrm{DIFF,AN}} = \frac{R_g \cdot T_{\mathrm{SOFC}}}{2 \cdot F} \ln\left[\frac{1-(JR_gT_{\mathrm{SOFC}}l_{\mathrm{AN}}/2FD_{\mathrm{eff,AN,H_2}}y^0_{\mathrm{H_2}}P_{\mathrm{SOFC}})}{1+(JR_gT_{\mathrm{SOFC}}l_{\mathrm{AN}}/2FD_{\mathrm{eff,AN,H_2O}}y^0_{\mathrm{H_2O}}P_{\mathrm{SOFC}})}\right]$ (V) (35) Cathode overpotential: $V_{\mathrm{DIFF,CA}} = \frac{R_g \cdot T_{\mathrm{SOFC}}}{4 \cdot F} \ln\left[\frac{1}{y^0_{\mathrm{O_2}}} - \left(\frac{1}{y^0_{\mathrm{O_2}}}-1\right)\exp\left(\frac{JR_gT_{\mathrm{SOFC}}l_{\mathrm{CA}}}{4FD_{\mathrm{eff,CA}}P_{\mathrm{SOFC}}}\right)\right]$ (V) (36) Total polarisation overpotential: $V_{\mathrm{PO}} = V_{\mathrm{DIFF,AN}} + V_{\mathrm{DIFF,CA}}$ (V) (37) Effective diffusion coefficient: $D_{\mathrm{eff},i} = \frac{D_{i,\mathrm{mix}}D_{i,\mathrm{K}}\varepsilon_{\mathrm{electrode}}}{(D_{i,\mathrm{mix}}+D_{i,\mathrm{K}})\tau_{\mathrm{electrode}}}$ ($\mathrm{m^2\,s^{-1}}$) (38)				
Properties	$D_{i,\mathrm{K}}$	$D_{i,\mathrm{mix}}$	$\varepsilon_{\mathrm{electrode}}$	$\tau_{\mathrm{electrode}}$	l_i
Evaluation [ref.]	Evaluation from [21] for 1×10^{-6} m pore size [45]	Evaluation from [21]	50% [45]	3 [45]	As in Table 7

Finally, the electrical efficiency of the SOFC, in respect to its fuel species input, is calculated, according to:

$$\eta_{\mathrm{el,SOFC}} = \frac{P_{\mathrm{SOFC}} - P_{\mathrm{COMP}}}{n^{\mathrm{in}}_{\mathrm{CH_4}} \cdot \mathrm{LHV}_{\mathrm{CH_4}} + n^{\mathrm{in}}_{\mathrm{H_2}} \cdot \mathrm{LHV}_{\mathrm{H_2}} + n^{\mathrm{in}}_{\mathrm{CO}} \cdot \mathrm{LHV}_{\mathrm{CO}}} \quad (41)$$

6.3. SOFC modelling results for operation with product gas

For the specified clean product gas composition of 26.15% H_2, 15.89% CO, 2.64% CH_4, 6.02% CO_2, and 49.1% H_2O that results from moistening the gasifier outlet, operating on STBR = 0.6, up to STCR = 2, several characteristic curves are drawn running the model at $T_{\mathrm{SOFC}} = 1173$ K and $P_{\mathrm{SOFC}} = 1.5$ bar. The following analysis shows the effect of product gas feed rate and fuel utilisation factor on the SOFC performance.

Increasing U_f results in excessive activation and Ohmic losses (Fig. 12) due to H_2 and especially O_2 partial pressure decrease at the end of the cell. The air inlet is preheated by the flue gas generated in a fluidised bed combustor instead of a SOFC post combustor. In the proposed system, O_2 partial pressures at the cathode exit are reduced more than in the usual SOFCs because less excess air is required in the fluidised bed combustor than would be required for cooling the SOFC post combustor. Accordingly, the air utilisation factor is higher in the present SOFC, resulting in lower exit O_2 partial pressures.

The combined effect is that the total electric power output versus current density reaches a maximum for any given U_f (Fig. 13). The maximum electric power output occurs at higher current densities for decreasing fuel utilisation factors because of lower activation overpotential losses. Nevertheless, low fuel utilisation factors are accompanied by a greater electric efficiency penalty. This is also shown in Fig. 14, which illustrates the electrical efficiency $\eta_{\mathrm{el,SOFC}}$, as defined in Eq. (41), versus the power produced for a wide range of fuel utilisation factors. The curve corresponding to $U_f = 0.7$ is presented with a dotted line to distinguish easily from the rest.

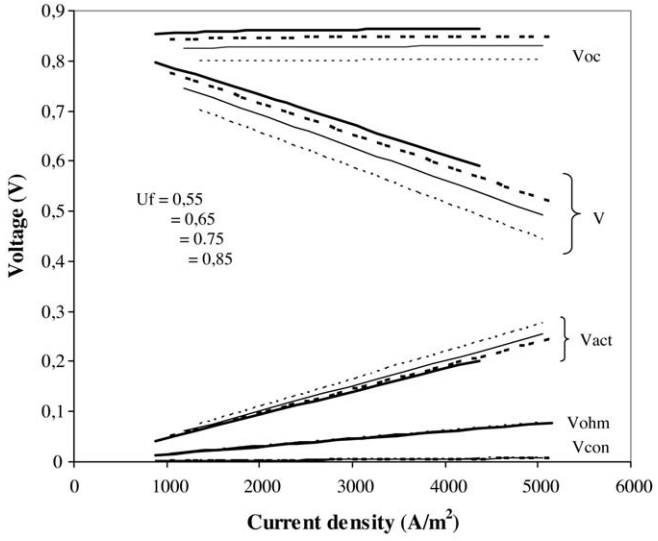

Fig. 12. SOFC voltage characteristics (V_{OC}, V, V_{OHM}, V_{ACT}, V_{PO}) vs. current density for different fuel utilisation factors.

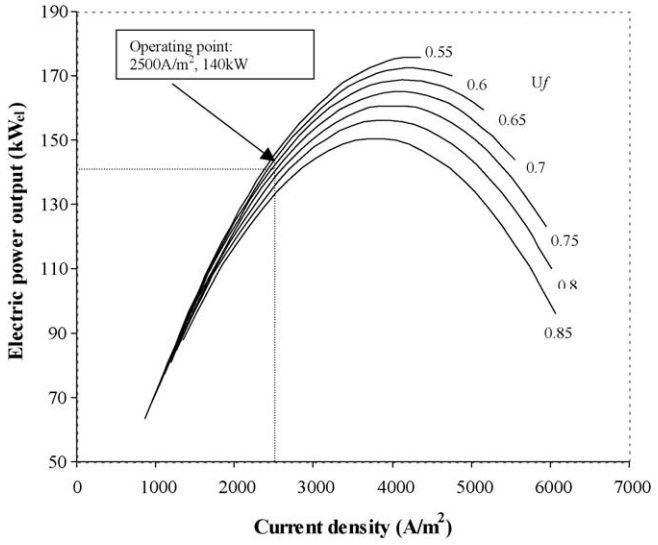

Fig. 13. SOFC stack power output vs. current density for different U_f values.

7. Integrated system results and discussion

The electrical efficiency of the integrated system, with respect to biomass fuel input, is defined as:

$$\eta_{\mathrm{el,CHP}} = \frac{n_{\mathrm{inv}} P_{\mathrm{SOFC}} - P_{\mathrm{COMP}}}{(\mathrm{Primary} + \mathrm{Secondary\ \ input\ \ biomass})_{\mathrm{LHV}}} \quad (42)$$

while thermal efficiency of the total system is defined as

$$\eta_{\mathrm{th,CHP}} = \frac{Q_{\mathrm{useful}}}{(\mathrm{Primary} + \mathrm{Secondary\ \ input\ \ biomass})_{\mathrm{LHV}}} \quad (43)$$

The definitions of the electrical efficiency of the integrated system $\eta_{\mathrm{el,CHP}}$ (Eq. (42)) and the electrical efficiency of the SOFC, $\eta_{\mathrm{el,SOFC}}$ (Eq. (41)), differ in what is considered as energy input. In Eq. (41) it is the fuel gas, in Eq. (42) it is the total biomass input to the gasifier and the combustor.

The anode depleted fuel combustion along with the unreacted char from the gasifier cannot sustain gasification for all the 50–200 kg h^{-1} primary biomass input range, for $U_{\mathrm{f}} > 0.7$ and additional biomass is required. This has a negative effect on the electrical efficiency of the integrated system $\eta_{\mathrm{el,CHP}}$ (Fig. 15) despite the fact that considering the stack separately, by plotting $\eta_{\mathrm{el,SOFC}}$, it operates more effectively at higher fuel utilisation factors (Fig. 14). In Fig. 15, the thick black line shows the curve for $U_{\mathrm{f}} = 0.7$ while the thick dashed line shows the thermal efficiency for $U_{\mathrm{f}} = 0.7$. It is evident that the electrical efficiency of the proposed system is optimised for a wide range of power outputs at $U_{\mathrm{f}} = 0.7$ reaching 45% for 80 kW$_{\mathrm{e}}$ net output and 25% for 160 kW$_{\mathrm{e}}$ net output. The corresponding thermal efficiency of the CHP system is also illustrated only for the optimised U_{f} ranging from 12 to 25%, respectively, considering as useful heat produced in the flue gas heat exchanger, in the form of hot water (HX4 in Fig. 1).

The presented analysis is not a total optimisation of the system for its nominal output value. The future cost of fuel cell stacks and other components compared with electricity and thermal energy revenues will determine the nominal capacity achieving best economical operation. Choosing an average

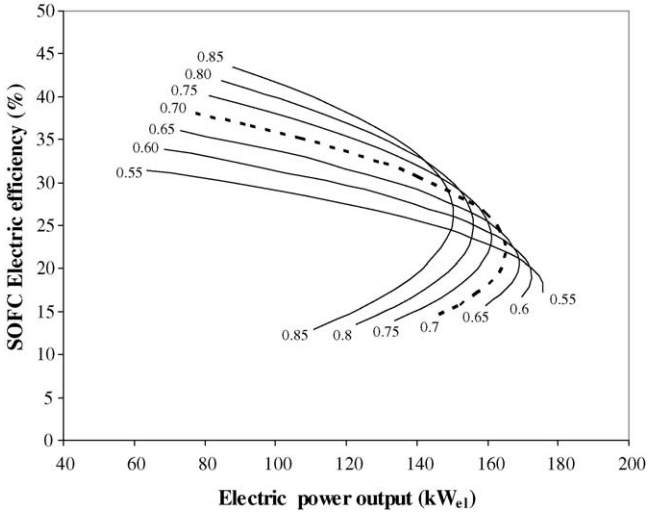

Fig. 14. SOFC efficiency vs. power output for different U_{f} values.

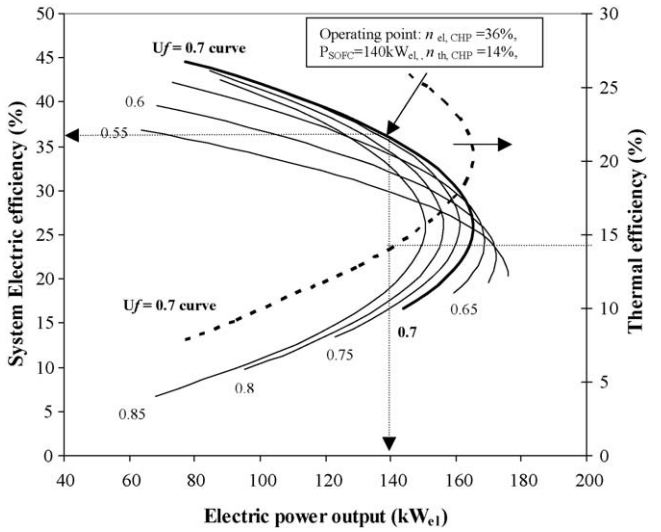

Fig. 15. CHP electrical efficiency vs. power output for different U_{f} values. Highlighted for optimised operation together with thermal CHP efficiency at $U_{\mathrm{f}} = 0.7$.

nominal current density value of 2500 A m^{-2}, at $U_{\mathrm{f}} = 0.7$, the system operates with ~36% electrical efficiency LHV producing 140 kW$_{\mathrm{e}}$ consuming 90 kg h^{-1} biomass. The system of Siemens Westinghouse exhibits a higher efficiency of 47% as stated in several published papers, e.g. [8] exhibits a higher efficiency of 47% but the fuel utilisation mentioned is around 85%. In our SOFC model, higher efficiencies can also be achieved by choosing different operating conditions, as shown in Figs. 13–15. Furthermore, in Van Herle et al. [48] who studied the utilisation of biogas in SOFCs, also state that SOFCs can achieve efficiencies in the range 30–40% in the power range 5–20 kW$_{\mathrm{el}}$.

For the evaluation of the total system all thermal, power and pressures losses for each unit operation were taken 2% of the input, which is a fair assumption compared to other SOFC system modelling works [8].

Further valuable results and discussion can be derived from an exergetic analysis of the plant presented in Part II of this work. The exergetic analysis can best illustrate the combined advantages of SOFC off gas utilisation for the allothermal gasification. A higher pressure system including an expander to drive the compressor will be investigated in the future and its implications to the total system will be assessed.

8. Conclusions

The combination of allothermal biomass gasification and SOFC for small scale CHP was assessed by modelling in Aspen Plus$^{\mathrm{TM}}$ process simulation software. The system operates on atmospheric pressure and is based on the novel "BioHPR" reactor, already proven for its capability to transfer required gasification heat between combustion and gasification fluidised beds by using high temperature heat pipes [6].

In the present modelling, this secondary fluidised bed is fed with SOFC depleted off gases, un-reacted gasification char and additional biomass if required. The number of heat pipes required for the thermal coupling of the two fluidised beds was

estimated at around 180 per MW_{LHV} gasifier biomass input. In order to avoid excessive number of heat pipes it was decided to use a low STBR = 0.6. The size of the system was based on the common 100 m^2 active surface SOFC. With average nominal current density 2500 A m^{-2}, at $U_f = 0.7$, the system operates with 36% electrical efficiency LHV producing 140 kW_e while the separate thermal efficiency is at 14%. The fuel utilisation factor $U_f = 0.7$ optimises total electrical efficiency over a range of power outputs. Higher U_f values necessitate additional biomass utilisation in the combustion FB and thus the efficiency drops.

The potential matching of SOFC fuel requirements and gasification product gas purity level by hot gas cleaning was investigated. High water concentrations inhibit effective H_2S removal at high temperatures. Lower temperatures result in poor efficiency and tar condensation problems. In Part II of the work the overall process is described with exergy terms to best illustrate its features.

References

[1] K. Maniatis, E. Millich, Energy from biomass and waste: the contribution of utility scale biomass gasification plants, Biomass Bioenergy 15 (1998) 195–200.

[2] S. Baron, N. Brandon, A. Atkinson, B. Steele, R. Rudkin, The impact of wood-derived gasification gases on Ni-CGO anodes in intermediate temperature solid oxide fuel cells, J. Power Sources 126 (2004) 58–66.

[3] O. Omosun, A. Bauen, N.P. Brandon, C.S. Adjiman, D. Hart, Modelling system efficiencies and costs of two biomass-fuelled SOFC systems, J. Power Sources 131 (2004) 96–106.

[4] M.A. Paisleya, M.C. Farrisa, J.W. Blacka, J.M. Irvingb, R.P. Overendc, Preliminary operating results from the Battelle/Ferco gasification, demonstration plant in Burlington, Vermont, USA, in: Presented at the First World Conference and Technology Exhibition on Biomass for Energy, Industry and Climate Protection, Seville, Spain, June, 2000.

[5] H. Hofbauer, R. Rauch, G. Loeffler, S. Kaiser, E. Fercher, H. Tremmel, Six years experience with the Ficfd-Gasification Process, in: Presented at the 12th European Conference and Technology Exhibition on Biomass for Energy, Industry and Climate Protection, Amsterdam, The Netherlands, June 17–21, 2002.

[6] EU Funded Project Biomass Heatpipe Reformer—Project Acronym: BioHPR Contract No. ENK5-CT-2000-0311.

[7] P. Costamagna, L. Magistri, A.F. Massardo, Design and part-load performance of a hybrid system based on a solid oxide fuel cell reactor and a micro gas turbine, J. Power Sources 96 (2001) 352–368.

[8] S. Campanari, Thermodynamic model and parametric analysis of a tubular SOFC module, J. Power Sources 92 (2001) 26–34.

[9] S.H. Chan, C.F. Low, O.L. Ding, Energy and exergy analysis of simple solid-oxide fuel-cell power systems, J. Power Sources 103 (2002) 188–200.

[10] Aspen Plus Physical Property Methods and Models Reference Manual, Aspentech®, 1999.

[11] M.J. Prins, K.J. Ptasinski, F.J.J.G. Janssen, Thermodynamics of gas-char reactions: first and second law analysis, Chem. Eng. Sci. 58 (2003) 1003–1011.

[12] J. Karl, Dezentrale Energie Systeme, Oldenbourg Verlag, München, 2004.

[13] C. Higman, M. Van Der Burgt, Gasification, Gulf Publishing, 2003.

[14] G. Schuster, G. Löffler, K. Weigl, H. Hofbauer, Biomass steam gasification—an extensive parametric modelling study, Bioresour. Technol. 77 (2001) 71–79.

[15] C. Pfeifer, R. Rauch, H. Hofbauer, In-bed catalytic tar reduction in dual fluidized bed biomass steam gasifier, Ind. Eng. Chem. Res. 43 (2004) 1634–1640.

[16] P.D. Dunn, D.A. Reay, Heat Pipes, fourth ed., Elsevier Science Ltd., Oxford, 1994.

[17] D. Kunii, O. Levenspiel, Fluidization Engineering, second ed., Butterworth, Heinemann, Boston, 1991.

[18] H. Martin, in: W. Vielstich, A. Lamm, H.A. Gasteiger (Eds.), VDI Heat Altas, John Wiley & Sons, 1993, pp. Mf1–Mf7.

[19] O. Molerus, A. Burschaka, S. Dietz, Particle migration at solid surfaces and heat transfer in bubbling fluidized beds. II. Prediction of heat transfer in bubbling fluidised beds, Chem. Eng. Sci. 50 (1995) 849–885.

[20] R. Peters, E. Riensche, P. Cremer, Pre-reforming of natural gas in solid oxide fuel-cell systems, J. Power Sources 86 (2000) 432–441.

[21] A.F. Mills, Heat and Mass Transfer, IRWIN, Chicago, 1995.

[22] J.K. Fink, L. Leibowitz, Thermodynamic and Transport Properties of Sodium Liquid and Vapor, Argonne National Laboratory Technical Report/ANL/RE-95/2, 1995 (available at: http://www.insc.anl.gov/matprop/sodium/sodiumdoc.pdf).

[23] S.Q. Turn, C.M. Kinoshita, D.M. Ishimura, J. Zhou, The fate of inorganic constituents of biomass in fluidized bed gasification, Fuel 77 (1998) 135–146.

[24] W. Wang, G. Olofsson, Reduction of Ammonia and Tar in pressurised biomass gasification. Fifth International Symposium on Gas Cleaning at High Temperatures, U.S. Department of Energy National Energy Technology Laboratory, Morgantown, WV, September 17–20, 2002 (available at: http://www.netl.doe.gov/publications/).

[25] K. Engelen, Y. Zhang, D.J. Draelants, G.V. Baron, A novel catalytic filter for tar removal from biomass gasification gas: improvement of the catalytic activity in presence of H_2S, Chem. Eng. Sci. 58 (2003) 665–670.

[26] J. Hepola, P. Simell, Sulphur poisoning of nickel-based hot gas cleaning catalysts in synthetic gasification gas. I. Effect of different process parameters, Appl. Catal. B: Environ. 14 (1997) 287–303.

[27] H. Kuramochi, W. Wu, K. Kawamoto, Prediction of the behaviours of H_2S and HCl during gasification of selected residual biomass fuels by equilibrium calculation, Fuel 84 (2005) 377–387.

[28] T.A. Milne, N. Abatzoglou, R.J. Evans, Biomass Gasifier 'Tars': Their Nature, Formation and Conversion, NREL Technical Report (NREL/TP-570-25357), 1998.

[29] L. Devi, K.J. Ptasinski, F.J.I.G. Janssen, S.V.B. van Paasen, P.C.A. Bergman, J.H.A. Kiel, Catalytic decomposition of biomass tars: use of dolomite and untreated olivine, Renewable Energy 30 (2005) 565–587.

[30] D. Dayton, Fuel Cell Integration. A Study of the Impacts of Gas Quality and Impurities Milestone Completion Report, NREL Technical Report/MP-510-30298, 2001.

[31] R.A. Newby, T.E. Lippert, R.B. Slimane, O.M. Akpolat, K. Pandya, F.S. Lau, J. Abbasian, B.E. Williams, D. Leppin, Novel Gas Cleaning/Conditioning for Integrated Gasification Combined Cycle, National Energy Technology Lab, Technical Report/AC26-99FT40674-02, 2001.

[32] EG & G Services, Parsons, Inc., and Science Applications International Corporation, Fuel Cell Handbook, fifth ed., DOE/NETL-2000/1110, National Energy Technology Laboratory, Morgantown, WV, 2000.

[33] D. Dayton, A Review of the Literature on Catalytic Biomass Tar Destruction Milestone Completion Report, NREL Technical Report/TP-510-32815, 2002.

[34] D. Sutton, B. Kelleher, J.R.H. Ross, Review of literature on catalysts for biomass gasification, Fuel Process. Technol. 73 (2001) 155–173.

[35] W.F. Elseviers, H. Verelst, Transition metal oxides for hot gas desulphurization, Fuel 78 (1999) 601–612.

[36] S.K. Gangwal, R. Gupta, W.J. McMichael, Hot gas cleanup-sulfur recovery. Technical, environmental and economic issues, Heat Recov. Syst. CHP 15 (1995) 205–214.

[37] K.R.G. Hein, A.J. Minchener, R. Pruschek, P.A. Roberts (Eds.), Integrated Hot Fuel Gas Cleaning for Advanced Gasification Combined Cycle Processes, JOULE II—Programme Clean Coal Technology R&D, vol. IV, Contract No. JOU2-CT93-0431, European Commission, 1998.

[38] A. Kohl, R. Nielsen, Gas Purification, fifth ed., Gulf Publishing Company, Huston Texas, 1997, pp. 1305–1307.

[39] A. Hidalgo, B.H. Cooper, High temperature fuel cells, in: W. Vielstich, A. Lamm, H.A. Gasteiger (Eds.), Handbook of Fuel Cells—Fundamentals,

Technology and Applications, vol. 3, John Wiley & Sons, 2003, pp. 186–187.

[40] J. Kapfenberger, J. Sohnemann, D. Schleitzer, A. Loewen, Acid gas removal by customised sorbents for integrated gasification fuel cell systems, 5th International Symposium on Gas Cleaning at High Temperatures, U.S. Department of Energy National Energy Technology Laboratory, Morgantown, WV, September 17–20, 2002 (available at: http://www.netl.doe.gov/publications/).

[41] S.A. Barnett, High temperature fuel cells, in: W. Vielstich, A. Lamm, H.A. Gasteiger (Eds.), Handbook of Fuel Cells—Fundamentals, Technology and Applications, John Wiley & Sons, 2003, pp. 1098–1108.

[42] E. Achenbach, E. Riensche, Methane/steam reforming kinetics for solid oxide fuel cells, J. Power Sources 52 (1994) 283–288.

[43] S.H. Chan, K.A. Khor, Z.T. Xia, A complete polarization model of a solid oxide fuel cell and its sensitivity to the change of cell component thickness, J. Power Sources 93 (2001) 130–140.

[44] S. Campanari, P. Iora, Definition and sensitivity analysis of a finite volume SOFC model for a tubular cell geometry, J. Power Sources 132 (2004) 113–126.

[45] A. Selimovic, Modelling of Solid Oxide Fuel Cells Applied to the Analysis of Integrated Systems with Gas Turbines, Doctoral Thesis, Department of Heat and Power Engineering, Lund University, Sweden, 2002.

[46] L. Magistri, R. Bozzo, P. Costamagna, A. F. Massardo, Simplified Versus Detailed Solid Oxide Fuel Cell Reactor Models and Influence on the Simulation of the Design Point Performance of Hybrid Systems, Trans. ASME 126 (July) 2004.

[47] E. Riensche, E. Achenbach, D. Froning, M.R. Haines, W.K. Heidugb, A. Lokurlu, S. von Andrian, Clean combined-cycle SOFC power plant—cell modelling and process analysis, J. Power Sources 86 (2000) 404–410.

[48] J. Van Herle, Y. Membrezb, O. Bucheli, Biogas as a fuel source for SOFC co-generators, J. Power Sources 127 (2004) 300–312.